

few particles. Removing them impairs the angular distribution, leading to anisotropic map resolution in 3D. Thus, 2D classification is best used to get rid of obvious non-protein particles, while leaving further cleaning to 3D classification.

3D classification, coupled with recent progress in *ab initio* 3D map generation (Punjani *et al* 2017), refines several (up to 10–20, depending on computational resources) 3D map classes by also adjusting the out-of-plane rotation of particles. This can be more useful for improving the results of CNN-based selectors, where most of the bad particles are dissociated-protein subunits rather than featureless contaminants (figure 4.5(b)). Such particles often average well in 3D and can be removed more reliably than in 2D. Furthermore, 3D classification initialized with low-resolution copies of the protein of interest can help remove particles belonging to the correct protein, but lacking high-resolution features, e.g. due to denaturation.

4.3 CTF estimation and image correction (restoration)

Benjamin A Himes and Nikolaus Grigorieff

Janelia Research Campus, Howard Hughes Medical Institute, Ashburn, VA, USA

Images recorded in the electron microscope have contrast that is affected by lens aberrations and imaging defocus (see section 1.2). These parameters may be manipulated by the microscope operator to enhance the contrast, in turn enabling 3D reconstruction of the object being imaged. Fortunately, lens aberrations and defocus do not lead to significant information loss thanks to the high degree of coherence of the electron beam. The relationship between lens aberrations and the contrast in the image is defined by the contrast transfer function (CTF). To calculate a 3D reconstruction, CTF effects will have to be accounted for. The more accurately the CTF is known, the higher the potential resolution of the reconstruction.

The CTF was introduced in section 1.2 as a function producing sinusoidal modulations of the elastic $F(s_x, s_y)$ structure factors and the amplitude damping factor $\mathcal{F}\{\mu\}$. The general assumptions underlying the theory presented in section 1.2 and here are as follows:

- i. The scattering is sufficiently weak that only interactions with the unscattered, incident beam must be considered, and further interactions of the specimen with already-scattered electrons can be ignored. This is known as kinematic scattering and leads to linear image formation.
- ii. The Fourier transform of the specimen potential is assumed to have Hermitian (Friedel) symmetry. This is only strictly true for a pure phase object, and it is approximately correct when the amplitude contrast is small.
- iii. A small amount of amplitude contrast, assumed to be 7%–10% for frozen-hydrated specimens, which only arises when nonlinear terms are considered, may be incorporated ad hoc in order to better match experimental data.

In the following description we will also ignore the frequency dependence of the amplitude term, as well as the variable amplitude losses with atom type. Given these simplifications, it is common practice to further assert that $\mathcal{F}\{\mu\}$ is proportional to $F(s_x, s_y)$ so that the amplitude-contrast ratio ‘ w ’ can be written as

$$\mathcal{F}\{\mu\}(s_x, s_y) = w/\sqrt{1-w^2}\mathbf{F}(s_x, s_y). \quad (4.1)$$

The approximation that the amplitude contrast is a constant does not limit the resolution in most cryo-EM experiments since amplitude contrast constitutes only a small fraction of the total contrast. Additionally, any errors due to this assumption can be partially compensated by adjusting the phase aberration function, $\gamma(s)$, which we discuss in the following section. Given equation (4.1) we write for the CTF (Wade 1992)

$$\text{CTF}(s) = -\sqrt{1-w^2}\sin\gamma(s) - w\cos\gamma(s). \quad (4.2)$$

The CTF is the Fourier transform of the objective lens point spread function, which causes delocalization of the signal in real space. This can be observed in figure 4.6

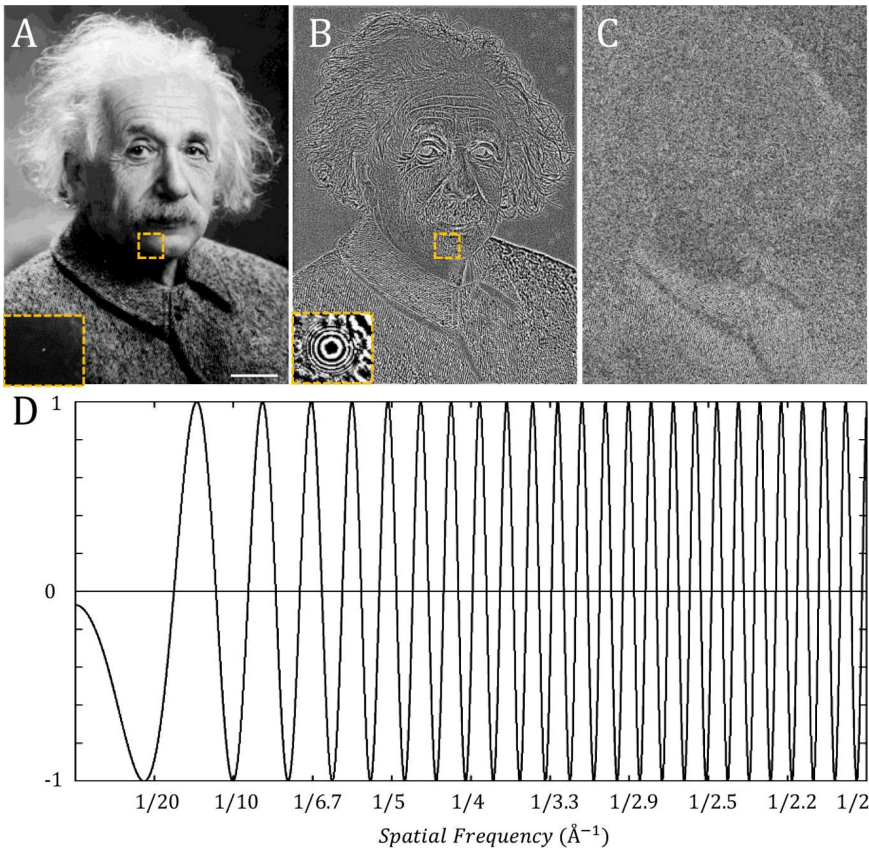


Figure 4.6. (A) Image of Albert Einstein (from Wikimedia Commons) with pixel size scaled such that his head is roughly the diameter of a ribosome. A particularly bright pixel is highlighted in the dashed orange box. Scale bar = 50 Å. (B) Image after application of a CTF that corresponds to a defocus of 1 μm. Information in the bright pixel is now delocalized by the point spread function, which displays alternating zones of positive and negative contrast, i.e. positive and negative deviations from the average intensity value. (C) Image at Scherzer defocus (~0.07 μm), showing reduced low-frequency contrast. (D) One-dimensional plot of the CTF at 1 μm underfocus. This image of Einstein has been included for illustrative purposes only; it has not been included for any promotional purposes, or to indicate any link between this publication and the Einstein estate.

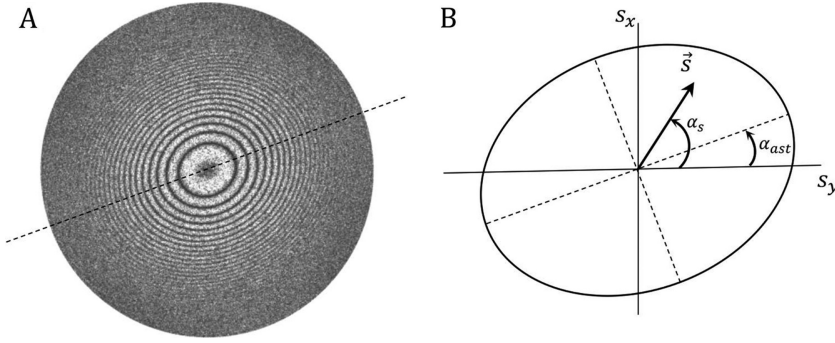


Figure 4.7. (A) 2D Thon ring pattern showing the sinusoidal oscillations that characterize the CTF, in this case with residual astigmatism resulting in an elliptical distortion. (B) Schematic showing the parameters describing the distortion due to astigmatism (equation (4.4)).

where the strong point feature in the panel (A) call-out box is shown, in panel (B), to be spread over many angstroms after application of the CTF. In addition to causing delocalization, the CTF also acts as a filter defined by zones of contrast reversal oscillating between -1 and 1 . This means that some spatial frequencies in an image, usually measured in \AA^{-1} , appear with unaltered contrast, others with inverted contrast, and some not at all when they are near a zero crossing of the CTF (figure 4.6(D)).

Furthermore, experimentally observed contrast transfer is characterized by a slowly varying attenuation toward higher spatial frequencies (larger values of s), commonly referred to as an envelope (sections 1.2 and 4.7). The attenuation can be the result of partial beam coherence as well as other systematic errors that will be discussed in section 4.8.

For the purpose of this section, we will only consider the combined effects of spherical aberration and defocus, including the presence of objective lens astigmatism, which leads to a dependence of the defocus on the two-dimensional (2D) Fourier coordinates s_x and s_y . We can rewrite $\gamma(s)$ as

$$\gamma(s_x, s_y) = 2\pi \left[\frac{C_s}{4} \lambda^3 s^4 - \frac{\Delta Z(s_x, s_y)}{2} \lambda s^2 \right], \quad (4.3)$$

where the astigmatism is parameterized according to the notion use in figure 4.7 and folded into the regular defocus term by

$$\Delta Z(s_x, s_y) = \frac{1}{2} [\Delta Z_1 + \Delta Z_2 + \Delta \Delta Z \cos(2[\alpha_s - \alpha_{ast}])] \quad (4.4)$$

with $\alpha_s = \tan^{-1} s_y/s_x$. In equations (4.3) and (4.4) ΔZ is the defocus at Fourier coordinates s_x and s_y , ΔZ_1 and ΔZ_2 are the maximum and minimum defocus values generated by the astigmatism, respectively, $\Delta \Delta Z = \Delta Z_1 - \Delta Z_2$, and λ the wavelength of the electrons. The spherical aberration constant¹ C_s is determined by the

¹ C_s can vary slightly with a change in the objective lens current, which changes the magnetic field inside the lens, however, this is negligible in practice.

design of the objective lens and, hence, the user can adjust the CTF primarily through changing the defocus and the wavelength. Most cryo-EM images are recorded at underfocus, which is achieved by weakening the objective lens, i.e. reducing its current. The imaged plane at focus under these conditions lies further from the objective lens and closer to the electron source in the microscope.

In equation (4.2) we see that the amplitude contrast term, $-w\cos\gamma$, is always negative for low spatial frequencies, which means imaging with overfocus would create an additional zone of weak contrast at very low spatial frequency ($s = \sqrt{2\Delta Z/C_s\lambda^2}$). To avoid this, cryo-EM data are commonly collected with an underfocused objective lens. By examining equation (4.3) we also see that underfocus can serve to partially cancel the effects of spherical aberration. A special focal condition that maximizes the width of the band of spatial frequencies prior to the first zero crossing of the CTF is called the Scherzer defocus (Scherzer 1949), $\Delta Z = -\sqrt{C_s\lambda}$. The effect of using Scherzer defocus for a weak phase object is illustrated in figure 4.6(C). While useful in material science applications, this imaging condition weakens low spatial frequency features that are important for particle alignment in cryo-EM. On the other hand, larger defocus enhances low spatial-frequency contrast and therefore helps in recognizing and aligning particles in an image. However, it also has the undesirable effect of reducing the spatial frequency of the first CTF zero, increasing the number of phase reversals in a given frequency interval, and leading to increased delocalization of the signal in real space due to the point spread function (see above). The latter is discussed further in section 4.3.2. In a single-particle experiment, it is therefore necessary to find a defocus, usually between 1 and 3 μm at 300 kV, that generates sufficient contrast while limiting detrimental effects.

4.3.1 CTF estimation

A full treatment of the effects of the CTF usually proceeds in two stages: CTF estimation and CTF correction. CTF estimation often makes use of the sinusoidal modulations predicted by equation (4.2), which were experimentally verified by Thon (1966, 1971) following theoretical work by Hanszen *et al* (Hanszen 1967, Hanszen and Morgenstern 1965). The sinusoidal modulations, sometimes referred to as Thon rings, form a characteristic pattern of rings or ellipses observed in computer-generated power spectra. They can be used to determine the defocus and astigmatism to within about 100 Å (Mindell and Grigorieff 2003), permitting 3D reconstruction at about 2 Å resolution (Jensen 2001). Once a reconstruction has been determined, the defocus parameters can be further refined and other, less significant errors can be measured and corrected (section 4.8). A full correction is therefore an iterative process that starts with an initial estimation of defocus and astigmatism from the electron micrographs themselves, without reference to a 3D reconstruction.

Figure 4.8(A) shows a typical power spectrum calculated from a cryo-EM image, highlighting Thon rings. These rings appear on a smoothly varying background (seen much more easily in a radial average of the 2D power spectrum), which decreases toward high spatial frequencies and which prevents the oscillations from

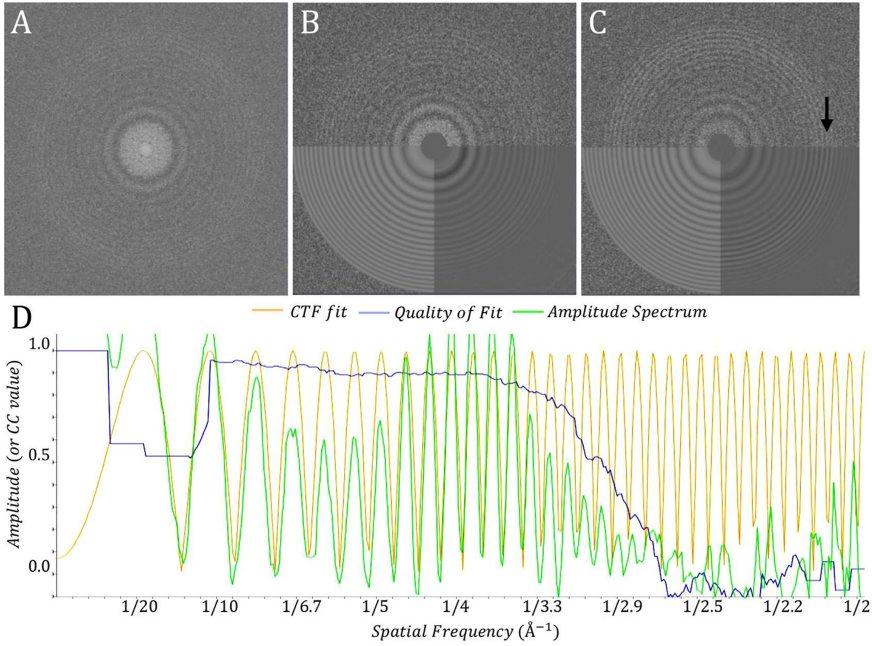


Figure 4.8. (A) Power spectrum calculated from an image of beta galactosidase (Bartesaghi *et al* 2015) after averaging the aligned movie frames (38 frames per movie at 1.2 electrons/Å²/frame). (B) Power spectrum after background subtraction and fitted with a calculated CTF (inset) (Rohou and Grigorieff 2015). (C) Power spectrum calculated as a sum of three-frame averages. The Thon rings are more clearly visible than in (A), particularly around the water ring at 3.7 Å resolution, marked by the black arrow. (D) 1D plot generated by CTFFIND4 (Rohou and Grigorieff 2015), showing the amplitude spectrum (green), the model fitted to the data (yellow), and a correlation-based score function (blue), which can be used to assess the spatial-frequency range that was fitted successfully (quality of fit > 0.5).

reaching zero. This background is primarily due to the noise associated with the detection of a given number of electrons (shot and detector noise), as well as contributions made by the usually ignored nonlinear terms to the image intensity, including the inelastically scattered electrons. After subtraction of the background term, which may be accomplished by a variety of approaches (Ludtke *et al* 1999, Penczek *et al* 2014, Sander *et al* 2003, Zhang 2016b, Rohou and Grigorieff 2015), the calculated CTF is compared to the observed power spectrum $A_d(s_x, s_y)$ between spatial frequencies s_{\min} and s_{\max} (figure 4.8(B)) by computing their cross correlation, given as

$$CC = \frac{\sum_{s_{\min} < |s| \leq s_{\max}} A_d(s_x, s_y) \cdot |CTF(s_x, s_y)|}{\sqrt{\sum_{s_{\min} < |s| \leq s_{\max}} A_d(s_x, s_y)^2 \cdot \sum_{s_{\min} < |s| \leq s_{\max}} |CTF(s_x, s_y)|^2}}. \quad (4.5)$$

A naïve approach to finding the best fit between the data and the model would involve an exhaustive search of all three parameters shown in figure 4.7(B). Since

this approach is computationally expensive, a ‘divide-and-conquer’ approach is adopted in many algorithms. For example, in the presence of moderate astigmatism an average defocus can be determined first by an exhaustive search of one parameter, followed by a local search to refine all three parameters including astigmatism (Zhang 2016b, Rohou and Grigorieff 2015). Some algorithms also estimate the astigmatism angle, α_{ast} , (equation (4.4)) by mirroring the power spectrum along the x - or y -axis and determining the rotation angle that aligns the mirrored version with the original in a one-parameter search.

To obtain an accurate fit and limit the effect of systematic errors and noise, the low spatial-frequency limit s_{min} is usually set to a value between 1/40 and 1/50 \AA^{-1} . This will exclude frequencies at which the contrast in cryo-EM images is affected by residual inelastically scattered electrons, a term that is not modeled correctly by equation (4.2). The optimal value for the high-frequency limit s_{max} depends on the strength of the Thon rings and background noise and it is usually set between 1/3 and 1/5 \AA^{-1} .

Apart from the envelopes that occur at higher resolution (section 1.2), the amplitude of the Thon rings is also affected by a limited depth of field (DeRosier 2000) in the case of thicker samples (section 4.8). Furthermore, Thon rings are attenuated by sample drift occurring during image acquisition, which leads to blurring in the image and loss of high-resolution signal in the direction of the drift. Thick samples (1000 \AA and more) will also reduce the visibility of Thon rings due to increased background and loss of electrons to inelastic scattering. For this reason, the strength and visibility of Thon rings often serves as a proxy to the overall quality of the data, an indicator that the data have the potential to yield a high-resolution reconstruction. While this criterion is often useful, weaker Thon rings may also simply be the result of fewer particles in the field of view, thus limiting the overall signal in the image that could otherwise be suitable for high-resolution reconstruction. The strength and visibility of the Thon rings can be quantified by cross-correlation with a calculated CTF (equation (4.5), figure 4.8(C)) (Rohou and Grigorieff 2015).

When micrographs are recorded as movies (section 3.5), blurring due to sample drift can be reduced by aligning the movie frames to each other to restore high-resolution contrast. With perfectly aligned frames, the contrast in the image, as well as the strength of the Thon rings, is maximized. However, movie alignment comes with its own errors and limitations, and local movement cannot always be fully corrected. It is therefore sometimes advantageous to calculate the power spectrum directly from the movie frames, or from sub-averages of multiple frames. In this case, the Thon ring pattern is the average of all calculated power spectra and, because it is calculated from multiple shorter time intervals, it is less affected by sample drift. For Thon rings generated by vitrified ice, an optimal interval for averaging is given by the time it takes to accumulate about 3–4 electrons/ \AA^2 (at 300 keV, figure 4.8(D)). At that point, the water molecules will have moved on average by about 1.5–2 \AA , which is still small enough to maximize the intensity of the Thon rings at a resolution of about 3–4 \AA (McMullan *et al* 2015).

Finally, most samples are tilted to some degree with respect to the optical axis of the microscope. This is done deliberately in a tomographic series, or it may be done to overcome limitations of preferred particle orientation (section 4.6, Tan *et al* 2017).

Even when sample tilt is not introduced intentionally, it is often present as a result of residual stage tilt or local sample undulations (Booy and Pawley 1993, Vonck 2000). Sample tilt leads to a variable defocus across the recorded image; to obtain a more accurate defocus estimate for each location, sample tilt axis and angle have to be determined in addition to the average defocus. This can be done, for example, by modeling the defocus variation across the image along a tilted plane (Mindell and Grigorieff 2003, Su 2019). More complex sample geometries may including tilt axis direction, tilt angle and other geometry descriptors as search parameters to achieve the best fit between locally calculated power spectra and corresponding CTF patterns (Tegunov and Cramer 2019).

The need for sample-tilt estimation depends on the degree of tilt. Defocus variation in images of nominally untilted samples can also be addressed on a per-particle basis by performing a local refinement of the defocus parameters against locally calculated power spectra (Zhang 2016b). When a 3D reference reconstruction is available, per-particle defocus values can be estimated by maximizing the correlation (or another similarity measure) between a particle image and a CTF-treated matching projection (Grigorieff 2007, Punjani *et al* 2017, Grant *et al* 2018, Zivanov *et al* 2018). This approach can also accommodate different particle heights in the ice layer of the sample (Noble *et al* 2018a). In this case, the signal available for per-particle CTF estimation is generated only by one particle and is therefore noisier than the signal in a Thon ring pattern calculated from a local patch or the entire micrograph. This increased level of noise imposes a lower molecular-mass limit on the particle of about 300–400 kDa. It also requires images with strong signal at spatial frequencies of at least $1/3$ – $1/4$ \AA^{-1} and a good reference reconstruction with corresponding resolution, below which errors in the estimation may be larger than the potential gain in defocus accuracy from per-particle CTF estimation.

4.3.2 Image correction

After determining the defocus and astigmatism values for each particle image, as well as particle orientations (Euler angles) and 2D coordinates within each image, a 3D reconstruction can be calculated (section 4.4). As discussed above, one of the features of the CTF affecting cryo-EM images are zones of weak or zero contrast. It is therefore impossible to fully restore the signal spectrum from a single image by simply dividing by the CTF. A partial correction that will not restore image amplitudes consists of restoring the phases of the spatial frequencies that were inverted by the CTF (phase flipping, van Heel *et al* 2000). To calculate a fully corrected reconstruction of the object, data from many images have to be merged (section 4.4), i.e. CTF correction and 3D restoration are accomplished in a single step. CTF correction can be illustrated by the simpler case of calculating 2D class averages (section 2.2), which lacks the 3D reconstruction step. A 2D class average is generated from a set of aligned cryo-EM images x_i ; $i \in M$ corresponding to the same particle view. It is convenient to refer to the Fourier transform of these images $X_i(s_x, s_y)$, which may be defined by the structure factor $F(s_x, s_y)$, corrupted by wave aberrations defined by the CTF and two additional noise terms (section 1.2):

$$X_i(s_x, s_y) = \text{CTF}_i(s_x, s_y) \cdot [\mathbf{F}(s_x, s_y) + \mathbf{N}_s(s_x, s_y)] + \mathbf{N}_i(s_x, s_y). \quad (4.6)$$

The noise terms $\mathbf{N}_i(s_x, s_y)$ represent different realizations of the ‘shot’ and detector noise in the particle images. In equation (4.6) ‘structural’ noise $\mathbf{N}_s(s_x, s_y)$ added by the embedding medium (ice), which is also affected by the CTF can also be considered but is often ignored. For images represented by equation (4.6) with $\mathbf{N}_s = 0$, Saxton (1978) derived a Wiener filter $\Omega(s_x, s_y)$ for TEM; optimal in the sense that it minimizes the sum of squared differences between the CTF-corrected average, $A_\Omega(s_x, s_y)$, and the underlying structure factor, $\mathbf{F}(s_x, s_y)$. Defining the ratio of particle signal power (before CTF aberrations) and average noise power $\sum_{i=1}^M |\mathbf{N}_i(s_x, s_y)|^2 / M$ as

$$\text{SNR}_{\mathbf{F}}(s_x, s_y) = \frac{M |\mathbf{F}(s_x, s_y)|^2}{\sum_{i=1}^M |\mathbf{N}_i(s_x, s_y)|^2}, \quad (4.7)$$

the Wiener filter is given by

$$\Omega(s_x, s_y) = \frac{1}{1 + 1/\text{SNR}_{\mathbf{F}}(s_x, s_y) \sum_{i=1}^M \text{CTF}_i^2(s_x, s_y)} \quad (4.8)$$

and the CTF-corrected, Wiener-filtered average is

$$\begin{aligned} A_\Omega(s_x, s_y) &= \frac{\sum_{i=1}^M \text{CTF}_i(s_x, s_y) X_i(s_x, s_y)}{\sum_{i=1}^M \text{CTF}_i^2(s_x, s_y)} \Omega(s_x, s_y) \\ &= \frac{\sum_{i=1}^M \text{CTF}_i(s_x, s_y) X_i(s_x, s_y)}{1/\text{SNR}_{\mathbf{F}}(s_x, s_y) + \sum_{i=1}^M \text{CTF}_i^2(s_x, s_y)}. \end{aligned} \quad (4.9)$$

$1/\text{SNR}_{\mathbf{F}}(s_x, s_y)$ was approximated by a constant in many early cryo-EM software packages, however, more rigorous statistical approaches (Scheres 2012a, Sindelar and Grigorieff 2012) now determine it as a function of the data. It can be seen that this term’s magnitude relative to the sum of squared CTF values (the second term in the denominator of equation (4.9)) is smaller the higher the ratio of structure factor to noise (equation (4.7)) and the larger the dataset (large M). In the limit of very large datasets, $\Omega(s_x, s_y) = 1$, and the CTF-corrected average will simply be a sum of CTF-multiplied images, divided by the sum of squared CTF values. If the CTF-corrected average, $A_\Omega(s_x, s_y)$, is estimated using a maximum likelihood approach,

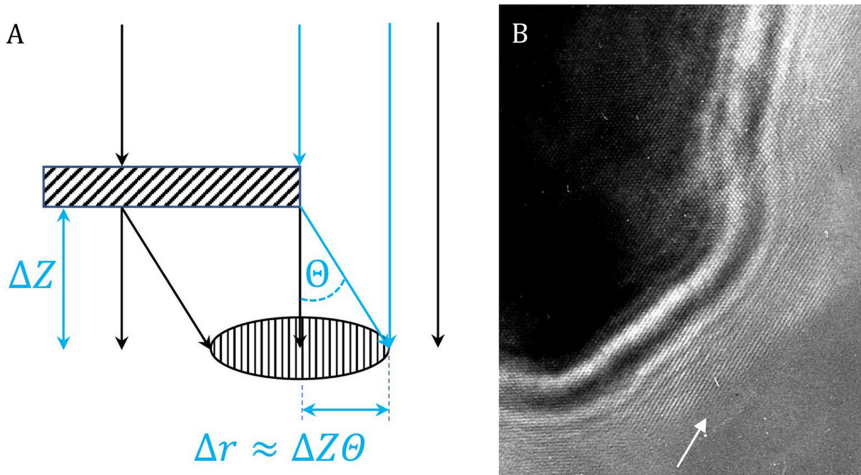


Figure 4.9. (A) Diagram explaining the displacement of signal from the edge of a particle. Phase contrast from the edge of the particle and corresponding to a spatial frequency $1/d$, where d is the resolution, will be displaced by $\Delta r = \Delta Z\Theta$, where ΔZ is the defocus and the scattering angle Θ is given by $\Theta \approx \lambda/d$, with λ the wavelength of the electrons ($\lambda \approx 1/50 \text{ \AA}$ at 300 keV). (B) Image of the edge of an InGaAs semiconductor crystal showing 3 \AA lattice fringes extending beyond the crystal edge due to an image defocus of about $1 \mu\text{m}$.

the terms in the sums in equation (4.9) are replaced by their probability-weighted estimates (Scheres 2012a, section 4.4).

Another result of the CTF-related degradation of images is the displacement (delocalization) of signal in real space, away from its location in a fully corrected image (see above). The amount of displacement, visible as Fresnel fringes in the images, is dependent on the spatial frequency of the signal, as well as the amount of image defocus. To fully recover the signal in a CTF-corrected average at a given resolution, d , it is therefore important that the window size used to extract particles from the micrographs is sufficiently large to include the fringes corresponding to the resolution d , as well as avoiding aliasing of the CTF oscillations in the Fourier transform (Penczek *et al* 2014). As a rule of thumb, the displacement of signal from the edge of a particle is given by the product of scattering angle, λ/d , and the defocus ΔZ (figure 4.9). To include these fringes for a particle with diameter D_p , the size of the window, D_w , should be at least

$$D_w = D_p + 2\frac{\lambda}{d}\Delta Z. \quad (4.10)$$

This means, for example, that 2 \AA signal in an image of a particle of 200 \AA diameter, recorded at 1 μm defocus and 300 kV requires a particle box size of about 400 \AA .

4.3.3 Magnification distortion

An additional source of image distortion that can limit the attainable resolution of a 3D reconstruction, and which therefore requires correction, is anisotropy in the image magnification (Grant and Grigorieff 2015, Zhao *et al* 2015). This ‘magnification

distortion', which usually affects only certain magnifications, is due to sub-optimal presets applied to the stigmators in the projector system of the microscope that require a service engineer and/or software update to rectify. The distortion leads to particles being stretched in one direction and compressed in the orthogonal direction compared to its average dimensions (figure 4.10(A)). The effect of magnification distortion on the final reconstruction depends upon the amount of stretching and compression, which can be up to a few percent, as well as upon the average particle diameter. For example, for a virus capsid with a 700 Å diameter, a 2% distortion (difference between most stretched and most compressed dimension) would lead to a displacement of the particle boundary from the particle center of $2\% \times 350 \text{ Å} = 7 \text{ Å}$, or about 3.5 Å from the

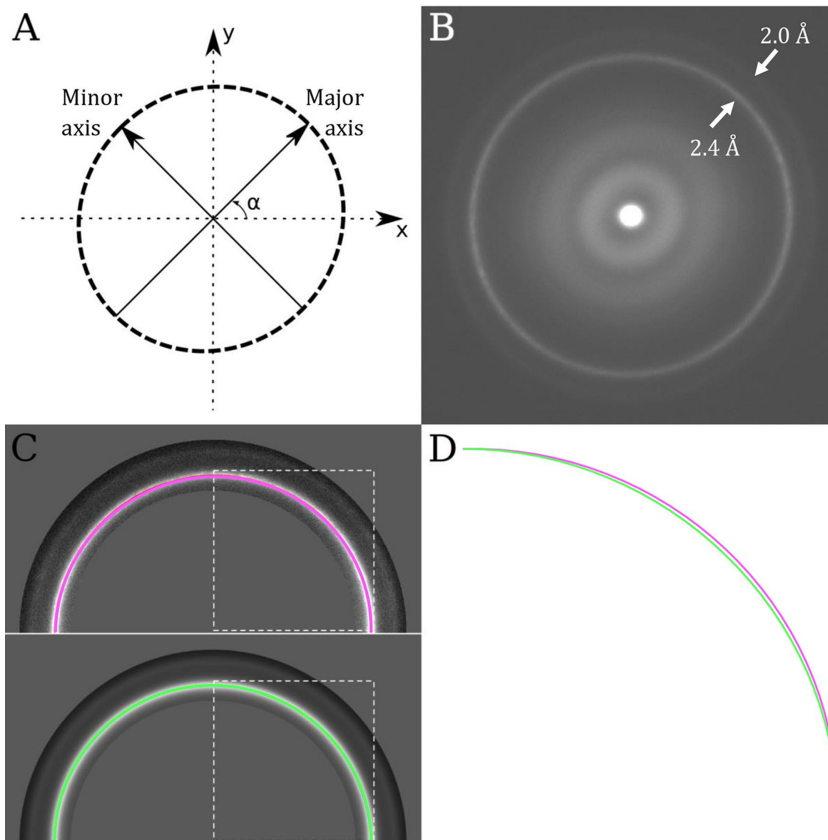


Figure 4.10. (A) Similar to axial astigmatism, magnification distortion can be parameterized by an ellipse; in this case an angle (α) and two scale factors along the major and minor axes. (B) Sum of the amplitude spectra from ten images of polycrystalline gold. Rings corresponding to spatial frequencies of at 2.4 and 2.0 Å are visible. (C) Top-half of the image shown in A, with the gold rings masked out and a path tracing the ~2.4 Å gold ring. Bottom-half of the rotational average of the image shown in (A), also with the gold rings masked out and a path tracing the ~2.4 Å gold ring. The dashed white box illustrates the area, which is shown zoomed in and overlaid in panel (C). (D) Overlay of the section of the paths traced in (B) surrounded by the dashed white box. A mismatch indicating a magnification distortion of about 2% is visible. Reproduced with permission from Grant and Grigorieff (2015). Copyright 2015 Elsevier.

average boundary position. An average 3.5 Å shift would eliminate signal beyond 7 Å resolution at the particle periphery in 2D class averages and 3D reconstructions, and severely attenuate signal at lower resolution.

The amount and direction of magnification distortion can be measured directly from the distortions observed in the particles (Yu *et al* 2016, Zivanov *et al* 2018), or from an image of a polycrystalline gold sample (figure 4.10(A)) (Grant and Grigorieff 2015). Since the distortion present in a given instrument does not change significantly over several months, it can be measured every few months, and images can be computationally corrected using the measured parameters by interpolation and resampling of the micrographs before proceeding with other steps in the image processing pipeline (Grant and Grigorieff 2015). The observed magnification distortion in instruments installed since the problem was recognized in 2015 has become less severe and correction may therefore not be required on newer instruments.

4.3.4 Concluding remarks

The steady improvement of algorithms has led to streamlined image processing of cryo-EM data, and many of the correction steps discussed here are now routine and fully automated. It also means that the demands on microscope hardware and operator skills in aligning instruments have been lowered. Most image distortions and misalignments can now be detected and corrected for by modern processing packages. Nevertheless, further improvement may come from making corrections for more complicated imaging errors, such as residual off-axis coma (Glaeser *et al* 2011) and for a small, defocus-dependent change in magnification when the electron beam is not completely parallel. Another source of error comes from inelastic scattering, which is currently not included in the correction of images, except for the ad hoc removal of background in power spectra (see section 4.3.1 above). The contribution of inelastically scattered electrons can be further reduced when an energy-filter is available. Additional correctors in the electron microscope, such as a chromatic aberration corrector, may convert some of the inelastically scattered electrons into electrons that contribute useful phase contrast to the image. This may then make additional algorithms necessary to accommodate this additional contrast.

4.4 Merging data from structurally homogeneous subsets

Basil J Greber

California Institute of Quantitative Biosciences (QB3), University of California, Berkeley, CA 94720, USA

Molecular Biophysics and Integrative Bio-Imaging Division, Lawrence Berkeley National Laboratory, Berkeley, CA 94720, USA

Present address: Institute of Cancer Research, Division of Structural Biology, Chester Beatty Laboratories, London SW3 6JB, UK

In this subsection, we will cover different aspects relevant to the three-dimensional (3D) reconstruction of a single cryo-EM map, preferably at high resolution, from a structurally homogeneous set of particle images. The methods employed to obtain homogeneous particle subsets from unclassified, heterogeneous cryo-EM datasets